Interference Effect of Wind on Thermal Power Plant Chimney

Rishabh Meena[1*] Himanshu Yadav[2*] Dr. Amrit Kumar Roy[3*]

[1*]*MTech, Structural Engineering, National Institute of Technology, Hamirpur, Himachal Pradesh-177005 (India)*
[2*]*PhD Scholar, Department of Civil Engineering, National Institute of Technology, Hamirpur, Himachal Pradesh-177005 (India)*
[3*]*Associate Professor, Department of Civil Engineering, National Institute of Technology, Hamirpur, Himachal Pradesh-177005 (India)*
Corresponding author, E-mail: 22mce104@nith.ac.in
ORCID: 0009-0009-1113-5297
Contributing author, E-mail: himanshu_phdce@nith.ac.in , amritroy@nith.ac.in

Abstract:

This paper is concerned with the interference effect of wind on the 198 m-tall industrial chimneys, located in Ferrybridge power station in West Yorkshire, England. Wind action has been the dominant consideration in the design of a power plant chimney. Calculating wind loads and their effects will require complicated wind tunnel testing. Wind tunnel investigation, hence, necessitates the measurement of wind loads on chimney models. Interference from the utility consideration aspect must be taken into consideration in the case of designing for high-rise constructions. The change in turbulence characteristics and mean wind velocity with height above the earth's surface is considered by this. CFD is therefore a great substitute for wind-based event prediction associated with chimneys or other such structures.

This master's final project aims to simulate the interference effect of wind on a power plant chimney due to its surrounding structures, which in this case is another chimney of the same dimensions and compare it with the effect of wind on an isolated chimney. In the first place, various sources were looked at to verify the model. After convergence studies about temperature, velocity, as well as pressure have been made. The dimensions of the chimneys in both versions were calculated following the latest state requirements. Also, a holistic explanation of the different steps (model geometry, meshing, and setup) was done to understand the study well. These outcomes are shown as contour, vector, etc. pictures.

Keywords: Chimney, Wind tunnel investigation, Interference, Turbulence, Wind velocity, CFD Simulation

1. Introduction

The modern world is moving further and faster requiring even more electricity. As such, power generation plants become more important and led further need for industrial chimney construction. A major purpose of a chimney is to dispose of those toxic and flu gases at relatively higher levels than possible. The gases must flow freely; therefore, chambers are often vertical or as close to vertical as is practicable. Chimneys were mainly used in factories, enterprises, and kitchens. Chimneys made of bricks, RCC steel, etc.., are available for purchase. Gases go outwards in the open as they escape through the chimneys. Moreover, the distribution and dispersal of pollutants towards higher altitudes

may also minimize their impact on the surrounding environment. Spreading the plants over a wider area reduces pollutant concentrations and helps meet regulatory limits.

The design of tall reinforced concrete chimneys using deterministic wind is highly advanced. Notable studies have been conducted on the ideal chimney shape (*Park et al. 2016*), condition assessment by modal testing (*Sancibrian et al. 2017*), seismic retrofitting (*Bru et al. 2017*), and the impact of wind on chimneys (*Karaca and Turkeli 2014, Liang et al. 2018*), in addition to the Indian Standard (IS) code (*IS 4998 I 2015*). The majority of these studies operate in the deterministic domain, which presupposes that all relevant parameters and load effects have constant values. However as has been shown time and time again, deterministic safety evaluations that ignore the uncertainty effect can have disastrous results (*Venanzi et al. 2015*).

Under irregular wind loadings, the best way of assessing the safety of a structure is through a fragility study. The probability that due to certain dynamic loads with certain intensities, a response quantity of both structural and non–structural systems will be beyond the critical threshold is what defines fragility. Many researchers have carried out WFA on many types of structures, such as wood frame constructions (*Lee and Rosowsky 2006*), freestanding steel towers (*Giaccu and Caracoglia 2018*), and container cranes (*Gur and Ray Chaudhuri 2014*). Here, it is necessary to mention the WFA of Southeast China's urban trees in high-wind regions (*Peng et al., 2018a*). Seismic fragility assessment of tall chimneys is a well-established area, but the WFA of chimneys research topic seems to be under-explored (*Zhou et al., 2015, Zhou et al., 2017*).

Doebling et al. (*1996), Sohn et al. (2004*), Carden and Fanning (2004), and Br Ownjohn (2007) are a few sources providing thorough evaluations of the research on system identification. Additional research on operational modal analysis of chimneys includes the following studies: Full-scale observations of chimney vibrations caused by wind were given by Ruscheweyh and Galemann (1996). The masonry chimney's operational modal analysis and FEM update were reported by Pallares et al. (2009), taking into account the influence of soil flexibility. System identification and FEM update for a reinforced concrete chimney were completed by Brownjohn et al. (2010). Breuer et al. (2015) measured a chimney's horizontal displacements and determined its modal values under various environmental circumstances.

1.1. State of the art

Continuous modifications have been made to chimneys ever since they were initially constructed in order to increase their efficiency and quality. Improvements often focused on insulating material.

Insulation goes back to the dawn of time when people created temporary dwellings and clothes from the same fibres. However, it was at the turn of the 1880s when thermal power plants started reducing excess heat loss through chimneys, heating systems, steam engines, and even surrounding buildings due to increased energy demands with rising coal and crude oil prices. As a result, new construction materials, including cast iron, glass buildings, concrete, and steel, were proposed as reasons why the first isolated chimneys originated during that time.

The chimneys that remain now are remarkable marvels of this kind of industrial brick architecture, constructed mostly of brick up until the mid-1900s. Later, the set was assembled as it rose in height using prefabricated concrete blocks that had been filled with concrete and matching steel rods (Construmatica, 2019).

However, stainless steel is increasingly gaining popularity in the modern world. This stems from its multitude of safety benefits, such as being exceptionally shock-resistant (chimneys do not crack or break down due to foundation settlements or even seismic movements). Additionally, stained steel is quite immune to soot fires, for which reason it is the most suitable. Similarly, stainless steel chimneys are environment-friendly owing to their thin walls (which conserve materials), chemical composition fitting for acid gas condensing boilers that generate hazardous fumes or condensate, full recyclability, and positive material value when the building's useful life ends.

Besides being a suitable heat-insulating material, the concept of a solar chimney for power generation has become more relevant today. Germany financed the one solar chimney pilot program built so far in Manzanares, Spain, during the time span 1981–1982 (*Breeze, 2016*).

A solar chimney refers to a vertically or horizontally buried solar air heater that is attached to a wall or roof. Typically, a chimney cavity has two walls: the first sheet is for absorbing heat, while the second one allows the sun's rays to penetrate.

Solar radiation enters the chimney cavity through the glass wall and heats up the air in buildings, thereby causing thermal buoyancy to push hot air upward, improving the natural ventilation of buildings. Conventional energy consumption is reduced through the employment of a solar chimney that encourages the natural chimney draft (*Shi, 2018*).

2. Description of the chimney

A 198-m high industrial chimney examined at Ferrybridge power station in West Yorkshire, England worked between the years 1927 and 2016 with a 34-m diameter at the ground level and 23-m outer diameter at the top level. Figure 1 depicts the view and longitudinal section of the chimney.

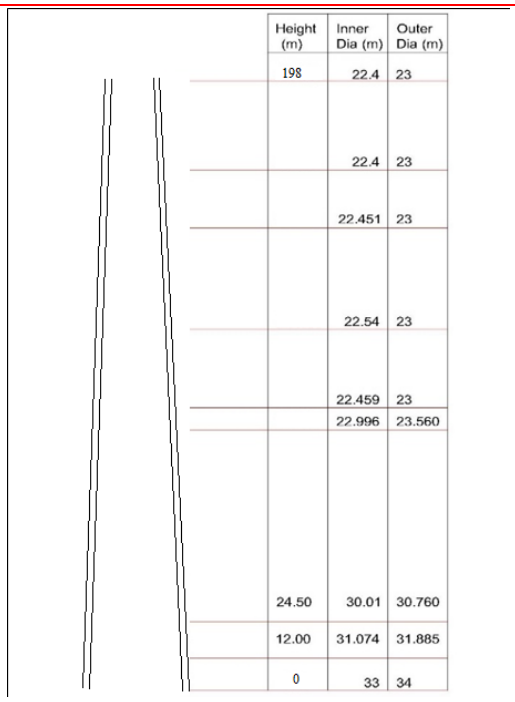

Figure 1. Industrial chimney of Ferrybridge power station: view and longitudinal section

The specifics of the prototype chimney and the wind conditions at the location, which led to the construction of models of the chimney and surrounding buildings and the execution of wind tunnel simulations, were considered in this study. The cross-section of the chimney resembles a ring.

The current study focuses on considering the influence of wind on a chimney. A rather stringent model was used for the study. Ratios were kept equal for the building model's geometric scale and intrinsic lengths of the model wind generated. Integral scales include inherent lengths of longitudinal component turbulence, roughness height, and depth of boundary layer. Some additional details relate to how large the test section is going to be, and what variables are to be considered. It should be noted that in this case, the test section of the wind tunnel will need to be excluded along with its walls.

3. Method

3.1. Specifics of the experimental setup's geometry meshing

Fine meshing is used on the chimney's interior and external surfaces, as well as in the vicinity of the bottom area that surrounds it. All models have a mesh quality that exceeds the value of 0.7. An element's quality is assessed using its Jacobian matrix determinant, which quantifies the distortions. It presents an ICEM-CFD value greater than 0.5, which shows the high quality of the mesh. As suggested by the CFD program, one can calculate the starting cell height using a number of computations. If the Reynolds number exceeds 5 x 10^5, the flow is termed turbulent across the surface. The majority of complications associated with wind flow are due to turbulence.

Following the computations, the mesh was constructed, and Figs. 2(a), (b), (c), and (d) display the side view, chimney with domain view, and a top view of the chimney model with interference, as well as the chimney model without interference.

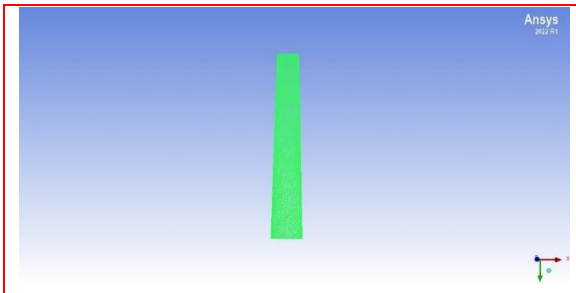

Figure 2(a). An image of the chimney model alone

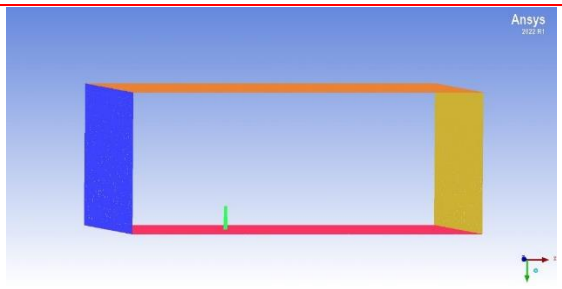

Figure 2(b). Isolated chimney model in a domain

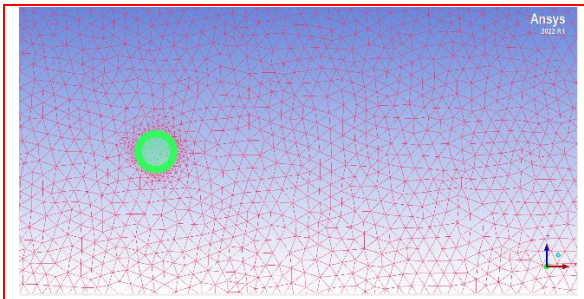

Figure 2(c). An isolated chimney model from the top

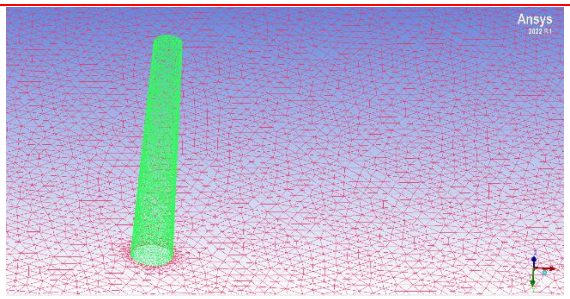

Figure 2(d). Model of an isolated chimney mesh

3.2 Domain Considered for CFD Modelling

3.2.1 Isolated Chimney Model

The isolated chimney's specifications, which were maintained throughout the wind tunnel experiment, remain unchanged. These dimensions are as follows: 198 meters for height, 34 meters for bottom diameter, and 23 meters for top diameter. Furthermore, the CFD simulation's chimney model with interference remains the same in terms of size.

The domain dimensions, or the cross-section of the wind tunnel employed in the CFD simulation, were considered.

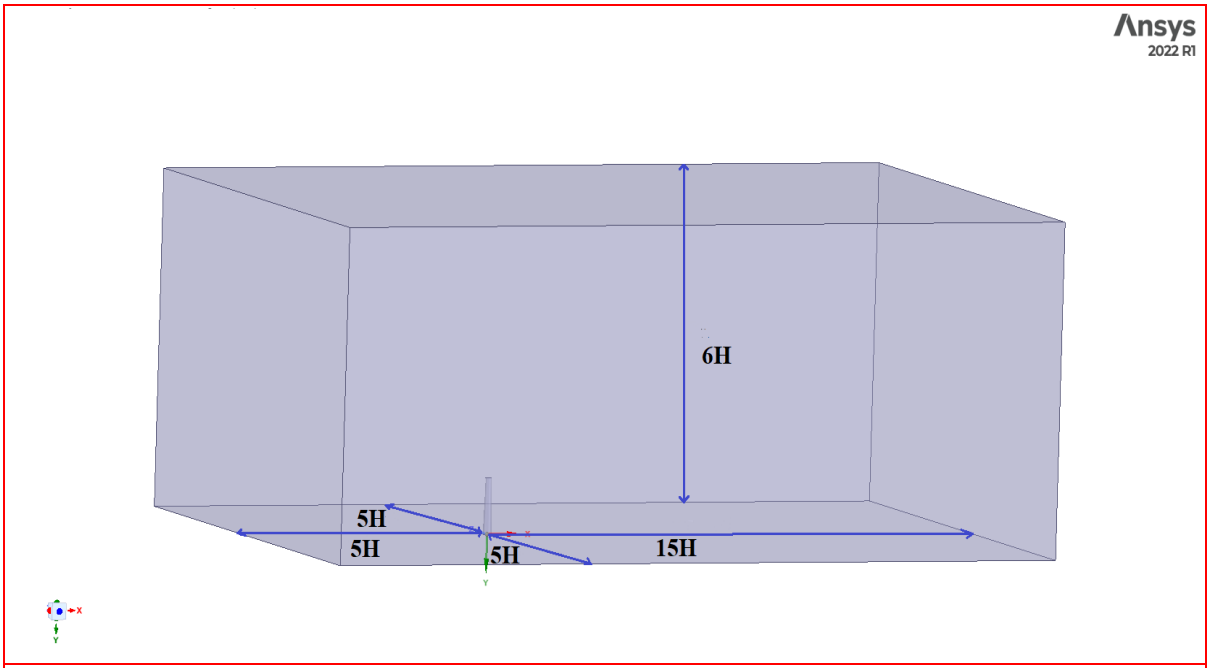

Figure 3. The computational domain of the chimney model employed in the CFD simulation. (Roy et al. 2012)

3.2.2 Chimney Model with Interference

Another chimney with the same dimensions that is 100 meters away from the main chimney is taken into consideration for interference analysis, and ICEM-CFD 2022 R1 is used for modelling and meshing.

Fig. 4 shows the schematic diagram of the chimney model used in the interference.

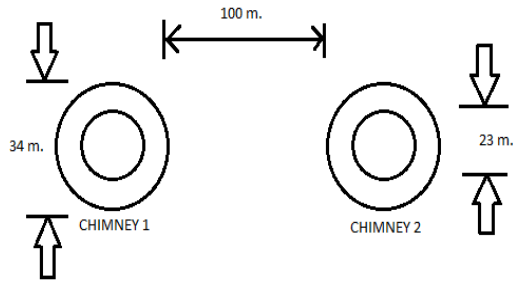

Figure 4. Principal chimney and interference chimney

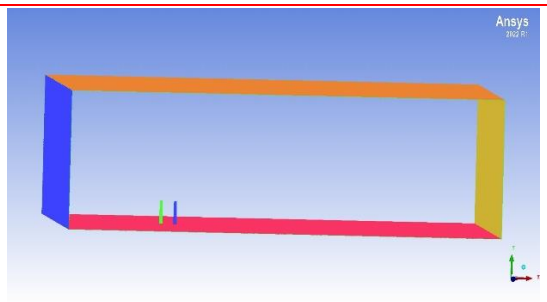

Figure 5(a). Interference chimney model in a domain

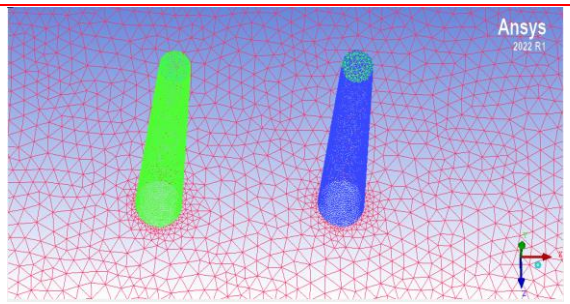

Figure 5(b). Model of an interference chimney mesh

As seen in Figure 5, the chimney was simulated in ICEM-CFD 2022 R1 considering the chimney as well as the other components as a single block, and the domain size as employed in an isolated chimney model was adjusted appropriately.

3.3 Turbulence Model

Previous studies (*Blocken, 2007a and 2007b*) have examined the relative applicability of numerous turbulence models for the airflow in the atmospheric boundary layer. It is a fact. It was observed that the most suitable solution for this sort of problem is the realizable k-model (*Shih et al., 1995*).

To solve the 3D problem, ANSYS Fluent 2022 R1, a commercial CFD code (ANSYS Ltd., 2022 R1) is utilized. Reynolds-averaged Navier-Stokes equations and the continuity equation: an approach to regulate volume. The realizable k-model is used to accomplish closure (*Shih et al. 1995*). Here pressure-velocity coupling is treated using the SIMPLE method. Second-order pressure interpolation is used. For the convective and viscous components of the governing equations, second-order discretization techniques are utilized.

3.4 Boundary Condition

It is not often easy to pinpoint the exact boundary conditions at the flow domain's entrance and departure that are required for a precise solution. This is because realistic physical representations of fluid flow require appropriate boundary conditions that genuinely mimic the real flow. The following formulas for the along-wind component of velocity, U, were utilized at the upwind boundary with a velocity inlet; these expressions are comparable to the results of the experimental investigation. The following illustrates how the velocity profile in the ABL is often represented.

$$U(z) = \frac{U^*}{k} \ln\left(\frac{z+z_0}{z_0}\right) \qquad (1)$$

The following are the values of the parameters used in this study: u = 0.11 meters per second, and z = 0.0002 meters. Eq. (2) is used to convert the measured longitudinal turbulence intensity (I) to turbulent kinetic energy (κ), which is then used as input for the simulations, provided that both σ_v and σ_w << σ_u. This is carried out in order to compare the turbulent kinetic energy (I) with the turbulent kinetic energy (κ). It should be noted that there is a little variance in the results as the amplification factors grow, on the order of a few percentage points (5%).

$$k(z) = \frac{u_*^2}{\sqrt{c_\mu}} \; or \; k(z) = 0.5(I_U U)^2 \qquad (2)$$

Richards and Hoxey (1993) provided the inlet turbulence dissipation rate profile ε, which is given by.

$$\epsilon(z) = \frac{u_*^3}{k(z+z_0)} \qquad (3)$$

The variables z, z_0 represent the height coordinate, scaled aerodynamic roughness length (z_0 = 0.03/150 = 0.0002m), and friction velocity associated with a horizontally homogenous (stable) ABL flow, respectively. The von Karman constant (~0:42) is represented by κ in this equation. To replicate the top and sides of the computational domain, slip walls (zero normal gradients for all variables and zero normal velocity) are employed. At the outlet, there is a specified zero static pressure. The standard coefficients of the realizable k- ε model were used. At the downwind boundary, a pressure outlet was used, with the inlet's backflow conditions for κ and ε and a relative pressure of 0 Pa. However, backflow was not seen in the domains because the downwind boundary was far enough from the chimney. To replicate the effect of the uneven ground, a rough wall was erected on the bottom wall of the domain. The input values K_S and C_S are necessary. By Blocken et al. (2007a), the roughness constant (K_S) in the law of the wall was defined as

$$k_s = \frac{9{\cdot}793}{C_s} z_0 = 3.98 \times 10^{-3} \qquad (4)$$

use the default value of 0.5 for C_S. The chimney's walls were intended to be smooth. Equations (2) to (3) were not used to characterize the initial conditions of the field parameters over

the whole domain at the beginning of the steady-state simulation. Common wall functions with roughness modifications are applied. As previously noted, an appropriate value of y+ (ranging from 30 and 300) for the employment of wall functions is established for the given simulation scale (1/150) utilizing the value specified for y+ and the underlying wind speed u0 from the wind tunnel research. The computational domain's bottom, which resembles the wind tunnel floor downstream of the degree of roughness sections, including the turntable, yields an estimated equivalent sand-grain roughness of 4 x 10-6m (modeling scale) or 0.0002m (full scale). The smooth floor's roughness is roughly represented by this number. This number is below the required threshold, yp (= 0.004 m, simulation scale).

3.5 Solver settings

ANSYS Fluent solves the associated problem-specific boundary conditions and the underlying governing equations via the finite-volume technique. The fundamental idea of the finite element approach is that the body is divided into small, distinct pieces called finite elements. Interpolation algorithms and nodes are used to specify these components. The governing equations for each element are specified, and the parts are assembled to form a bigger matrix. As was already said, the replies were in a constant condition. For the pressure, momentum, and turbulence equations as well as the "coupled" pressure-velocity coupling approach, second-order differencing was used because of its dependability for steady-state, single-phase flow problems. The residuals failed to recover to 104 of their initial values after many hundred cycles, which is a well-recognized criterion. Until the forces operating on the chimney—drag, lift, side, and moment—reached stationary values, the models were not considered to have converged. Despite the steady state of the simulations, there was a 1% fluctuation in the "steady" values of the several monitoring metrics.

4. Result

4.1. Validation of the Pressure Coefficient and the ABL

The local mean wind speed and the turbulence intensity of the incoming flow are required to build a user-defined function for the kinetic energy and energy dissipation rate (e) of the wind flow. The CFD simulation's velocity profile and the real data were found to be quite comparable. Pressures at various locations were monitored in a natural sequence using the developed data collection system software. The following is a dimensionless expression for wind pressures at various spots on the model:

$$C_P = \frac{p - p_s}{0{\cdot}5\rho V^2} \qquad (5)$$

Here,

C_p = Pressure coefficient in this case.

P = Model's measured surface pressure.

P_s= Static pressure in the free stream.

V = Model's top free mean wind speed.

ρ = Air Density

To compute wind pressures on the outside surface of the chimney, two polylines were taken into consideration for the Plane and boundary intersection vertical plane on the YZ-axis in CFD-Post. In Figure 6, these polylines are displayed. Figs. 6 depict the various sides of the outside surface of the industrial chimney. The pressure contours along their faces are seen in these figures.

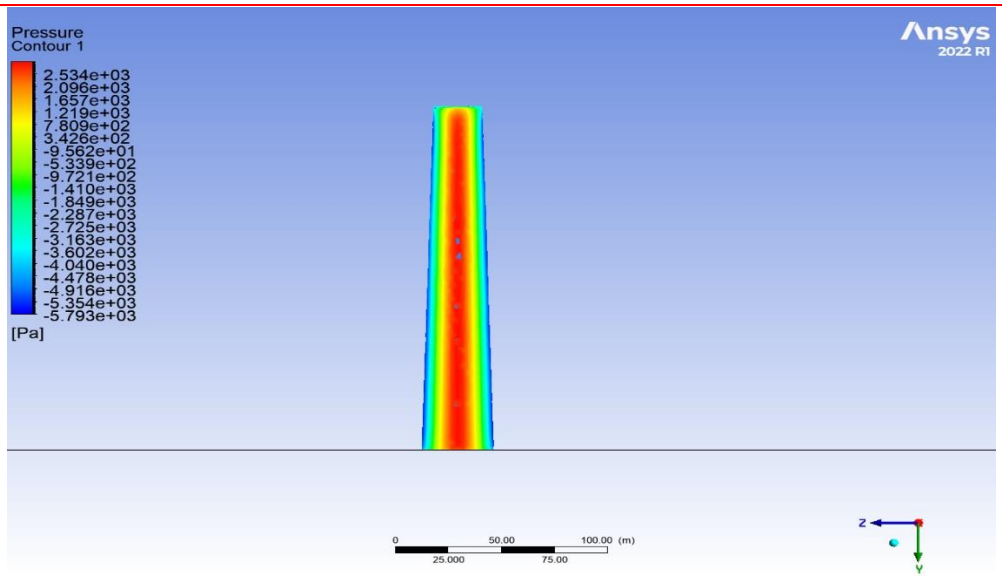

(a)

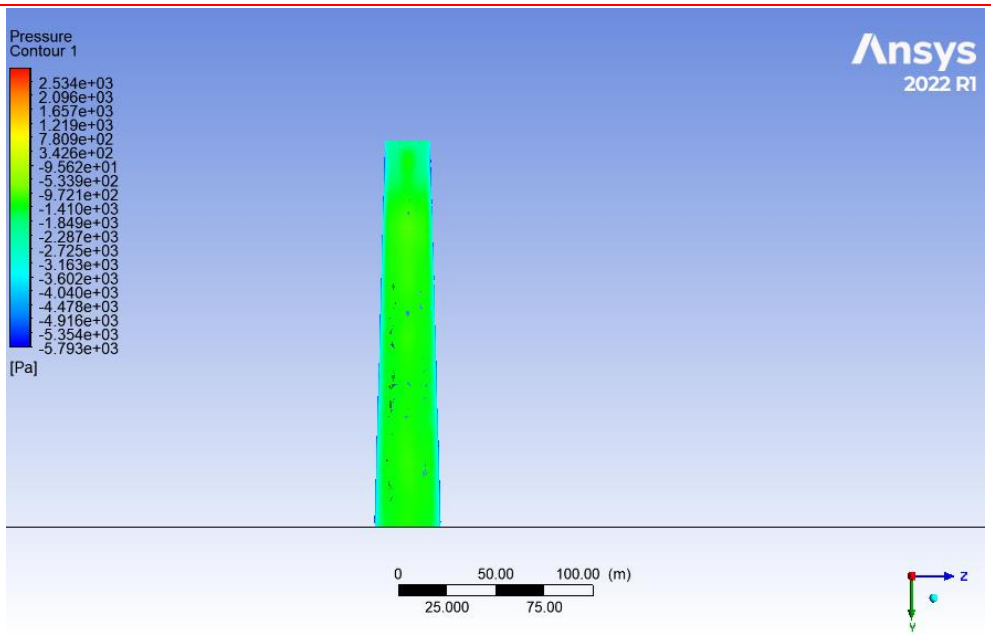

(b)

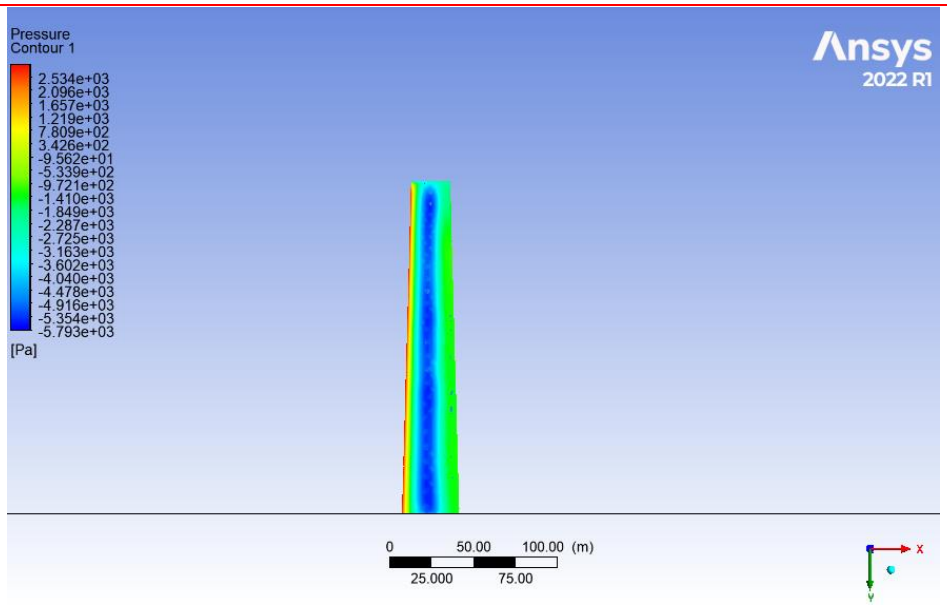

(c)

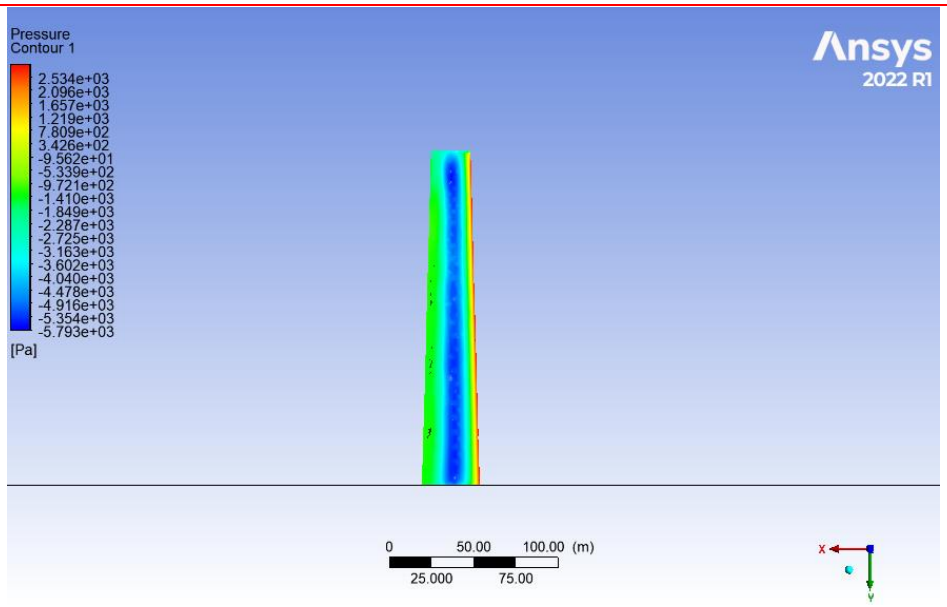

(d)

Figure 6. Contours of Pressure Coefficient at (a) front-side, (b) back-side, (c) left-side and (d) right-side of the isolated chimney model.

4.2. Vector field of velocity

The flow of fluid is defined as a three-dimensional velocity vector field in terms of continuum mechanics. As the flow changes over time, the field lines derived from the vector field description of the flow diverge. A streamline's curvature is affected by pressure gradients acting perpendicular to it. The streamline's plane of curvature is found in the path of radial pressure decrease. The magnitude of the radial pressure gradient may be calculated directly given the fluid density, streamlined curvature, and local velocity. The streamlined results of the airflow within the domain are additional information that the solution could produce. Our streamlines may be shown below in Figure 7,

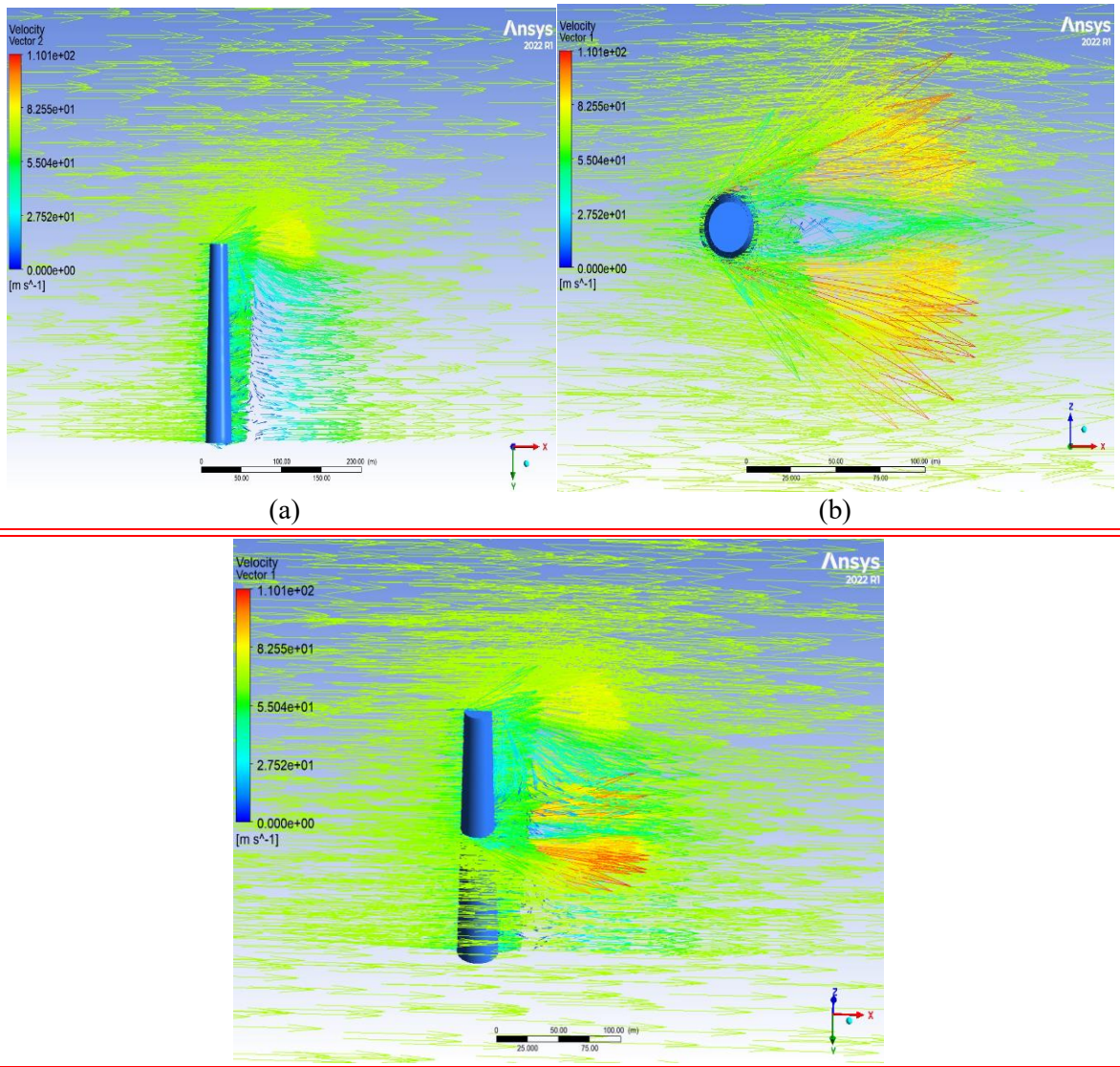

Figure 7. Flow pattern and vortex formation in isolated chimney model subjected to wind.

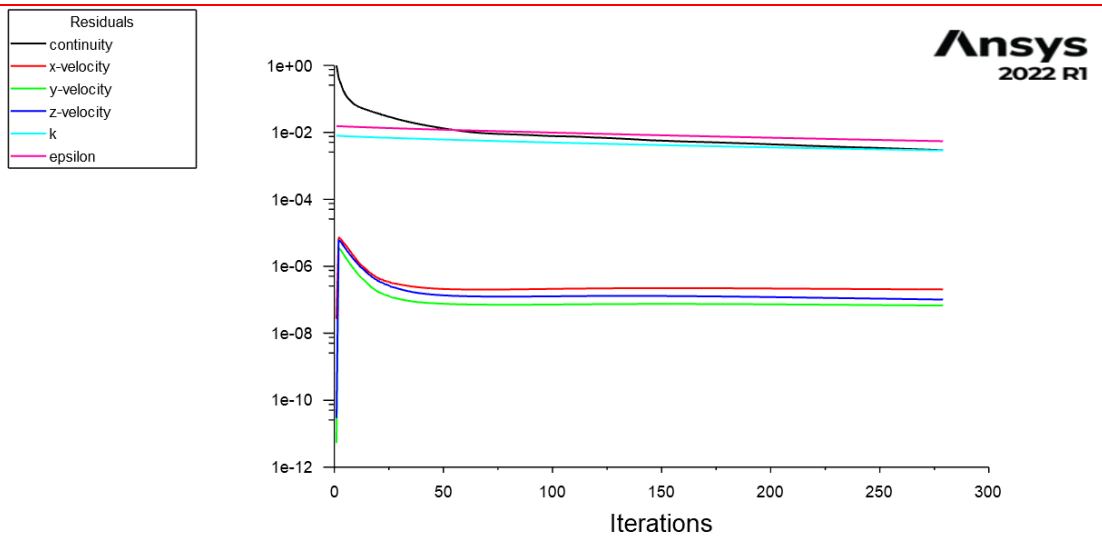

Figure 8. Graph of scaled residue of isolated chimney

Now, comparing the results of isolated chimney model with the interference effect chimney we have following results for interference chimney:

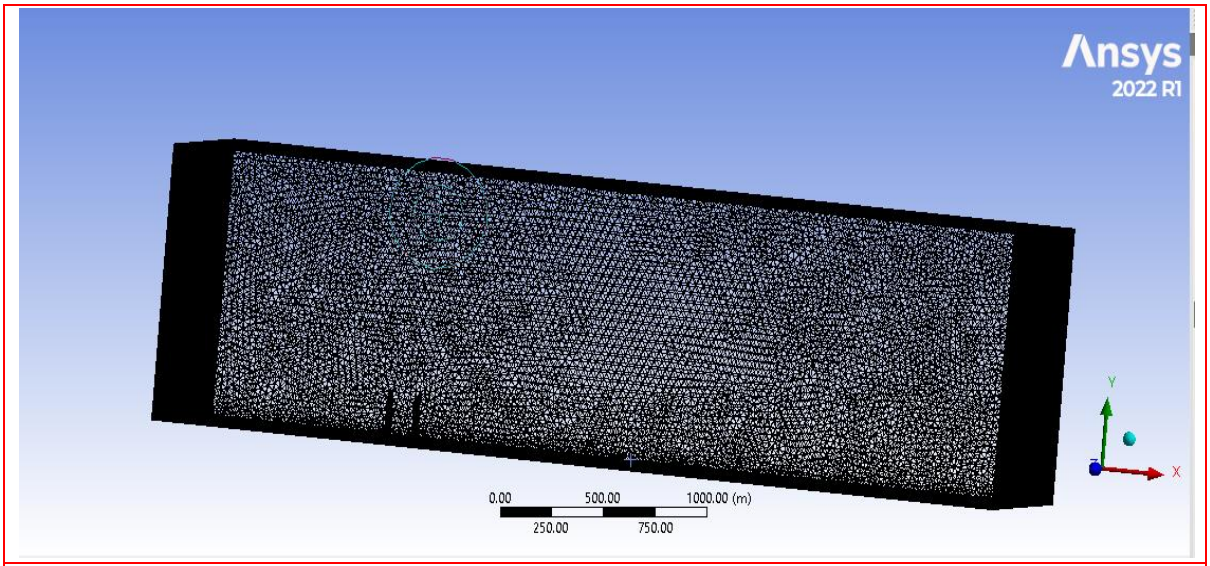

Figure 9. Meshing of both chimneys and the domain

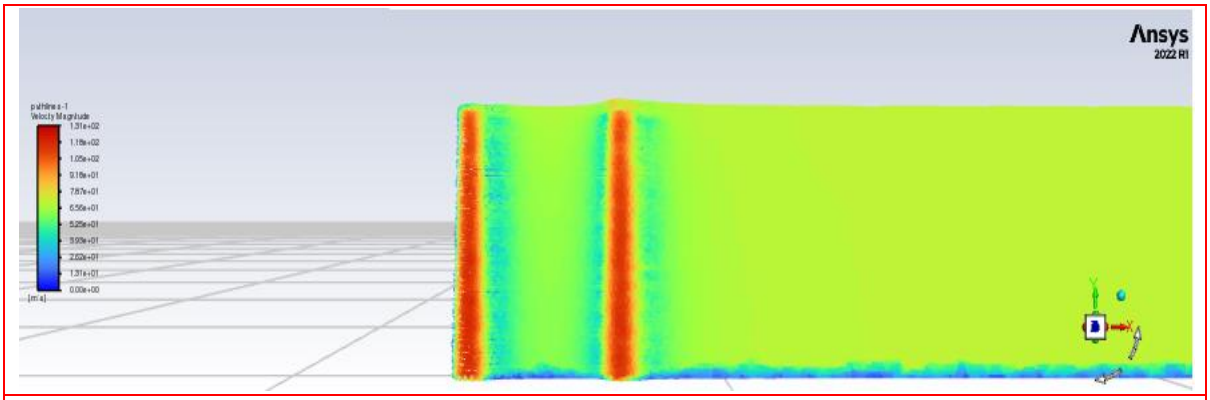

Figure 10. Velocity magnitude pathlines for interference model

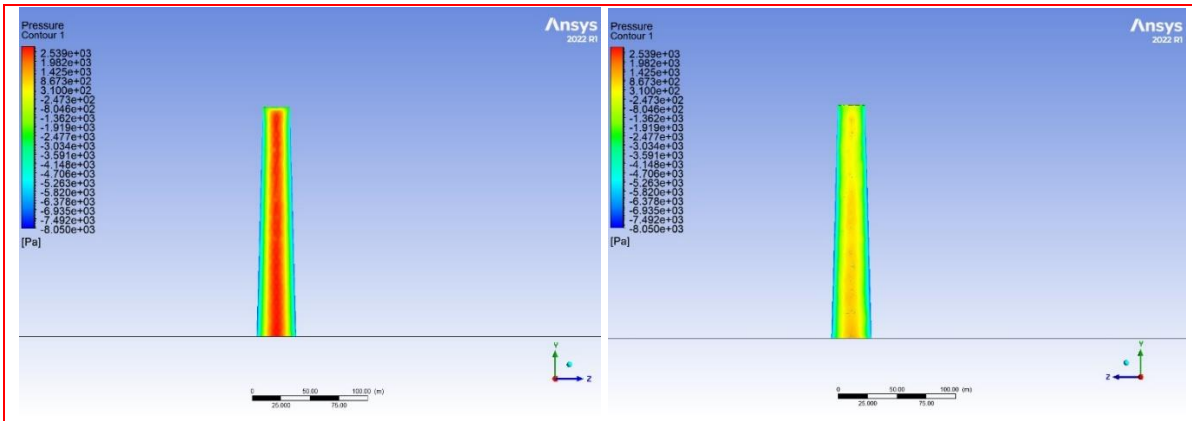

11(a) 11(b)

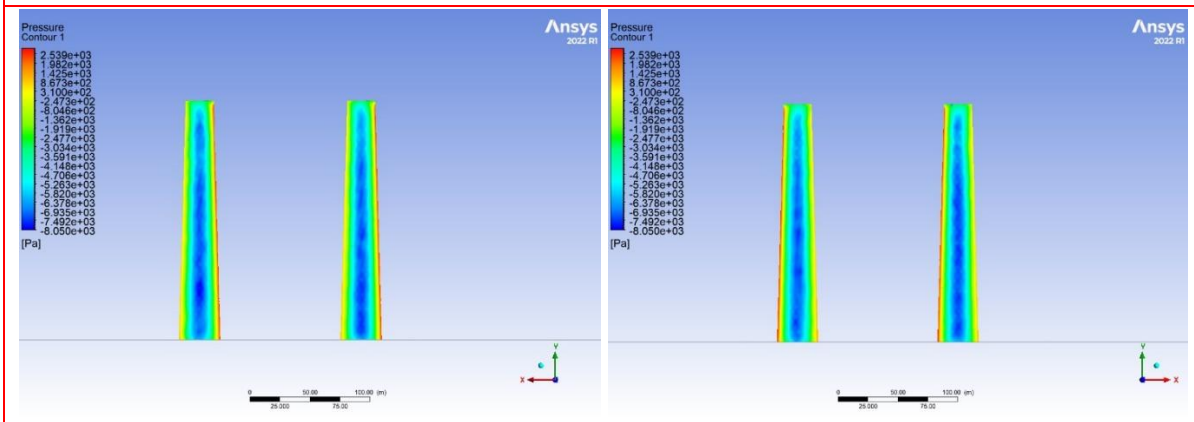

11(c) 11(d)

Figure 11. Contours of Pressure Coefficient at (a) front-side, (b) back-side, (c) left-side and (d) right-side of the interference chimney model

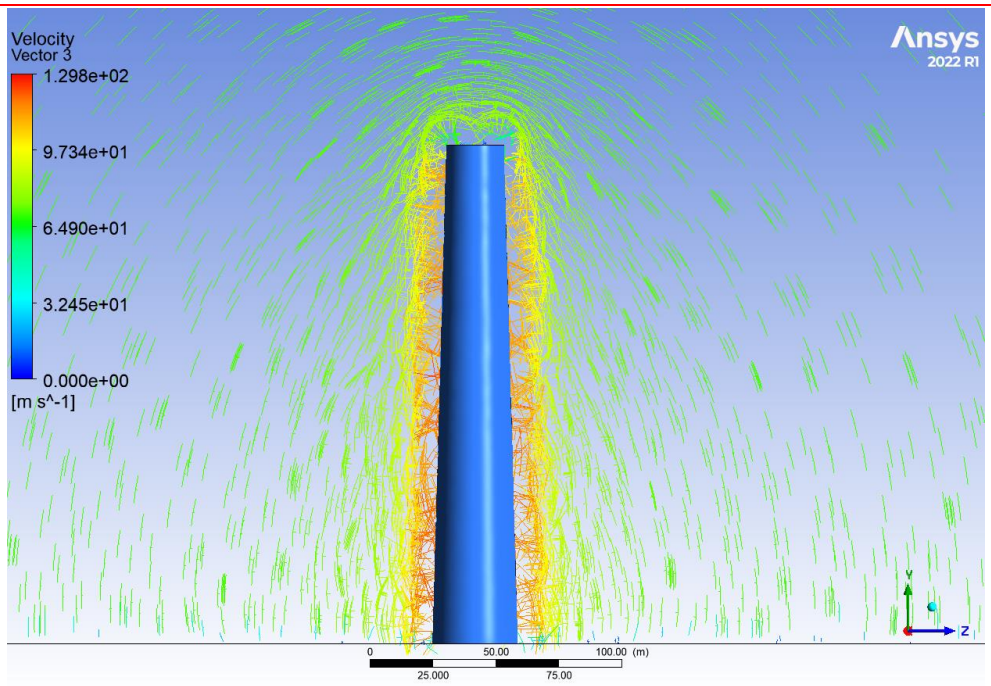
Velocity
Vector 3
1.298e+02
9.734e+01
6.490e+01
3.245e+01
0.000e+00
[m s^-1]
Ansys
2022 R1
0
50.00
100.00 (m)
25.000
75.00
Y
Z

12(a)

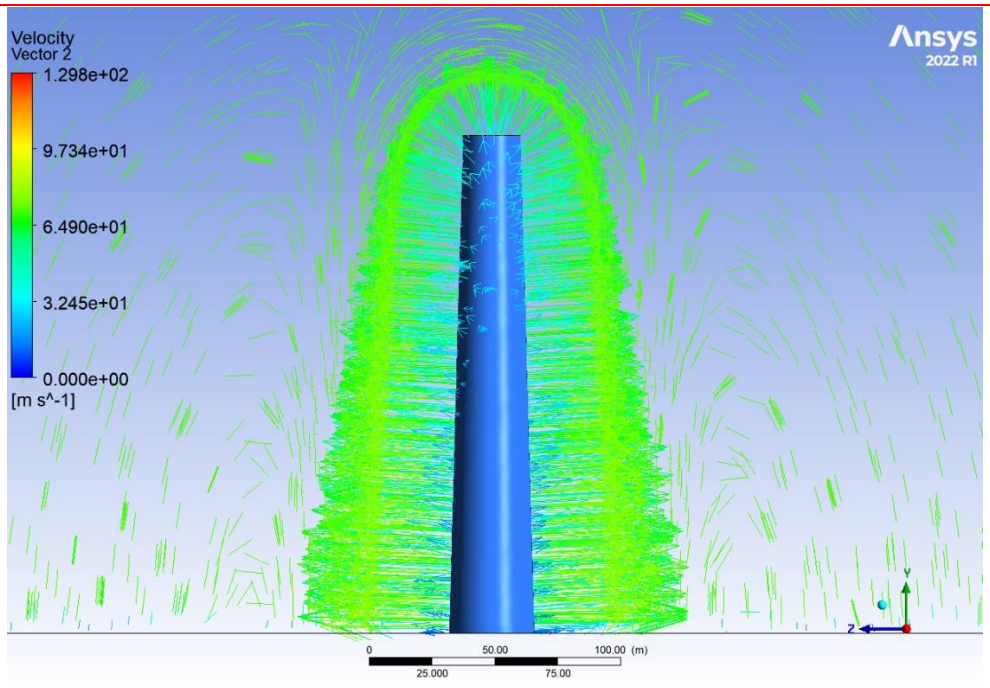
Velocity
Vector 2
1.298e+02
9.734e+01
6.490e+01
3.245e+01
0.000e+00
[m s^-1]
Ansys
2022 R1
0
50.00
100.00 (m)
25.000
75.00
Y
Z

12(b)

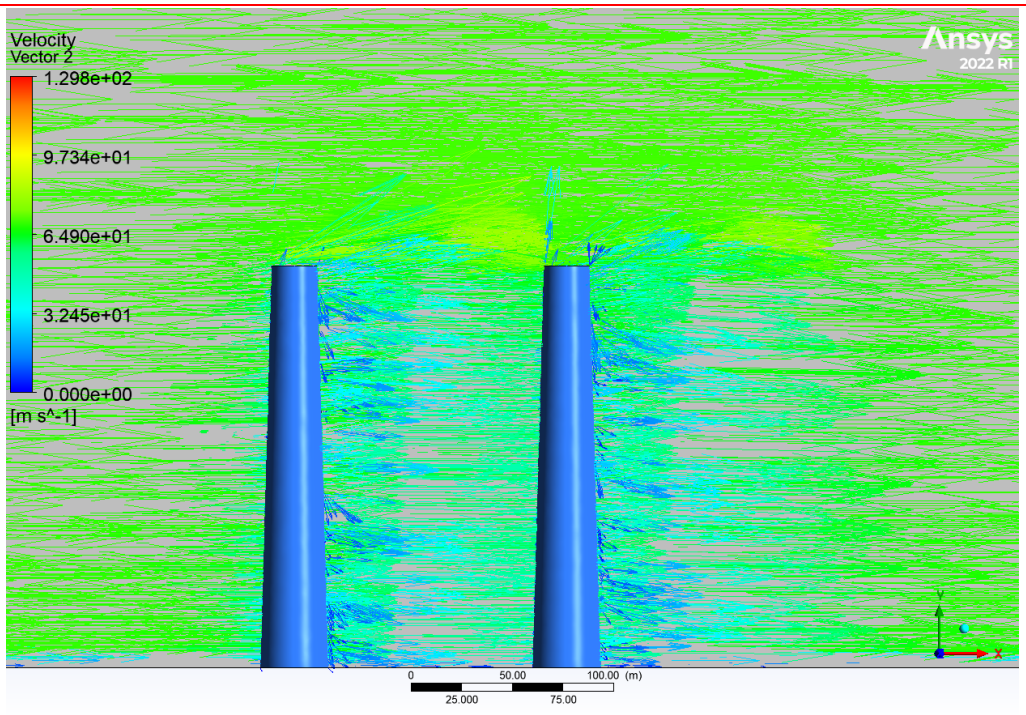
Velocity
Vector 2
1.298e+02
9.734e+01
6.490e+01
3.245e+01
0.000e+00
[m s^-1]
Ansys
2022 R1
0
50.00
100.00 (m)
25.000
75.00
Y
X

12(c)

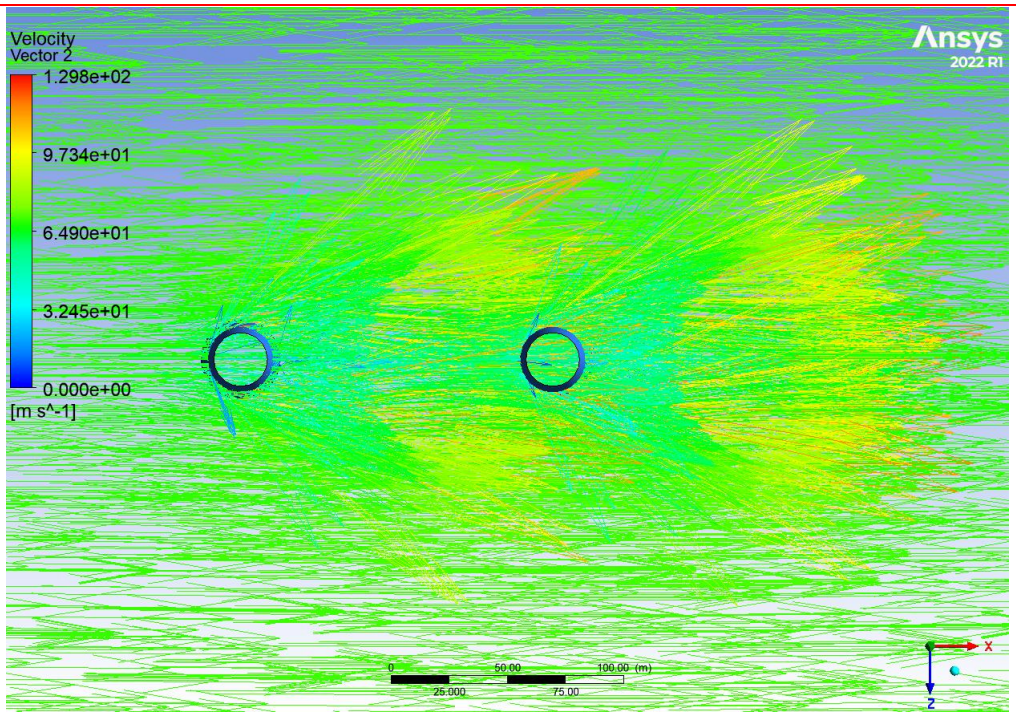
Velocity
Vector 2
1.298e+02
9.734e+01
6.490e+01
3.245e+01
0.000e+00
[m s^-1]
Ansys
2022 R1
0
50.00
100.00 (m)
25.000
75.00
X
Z

12(d)

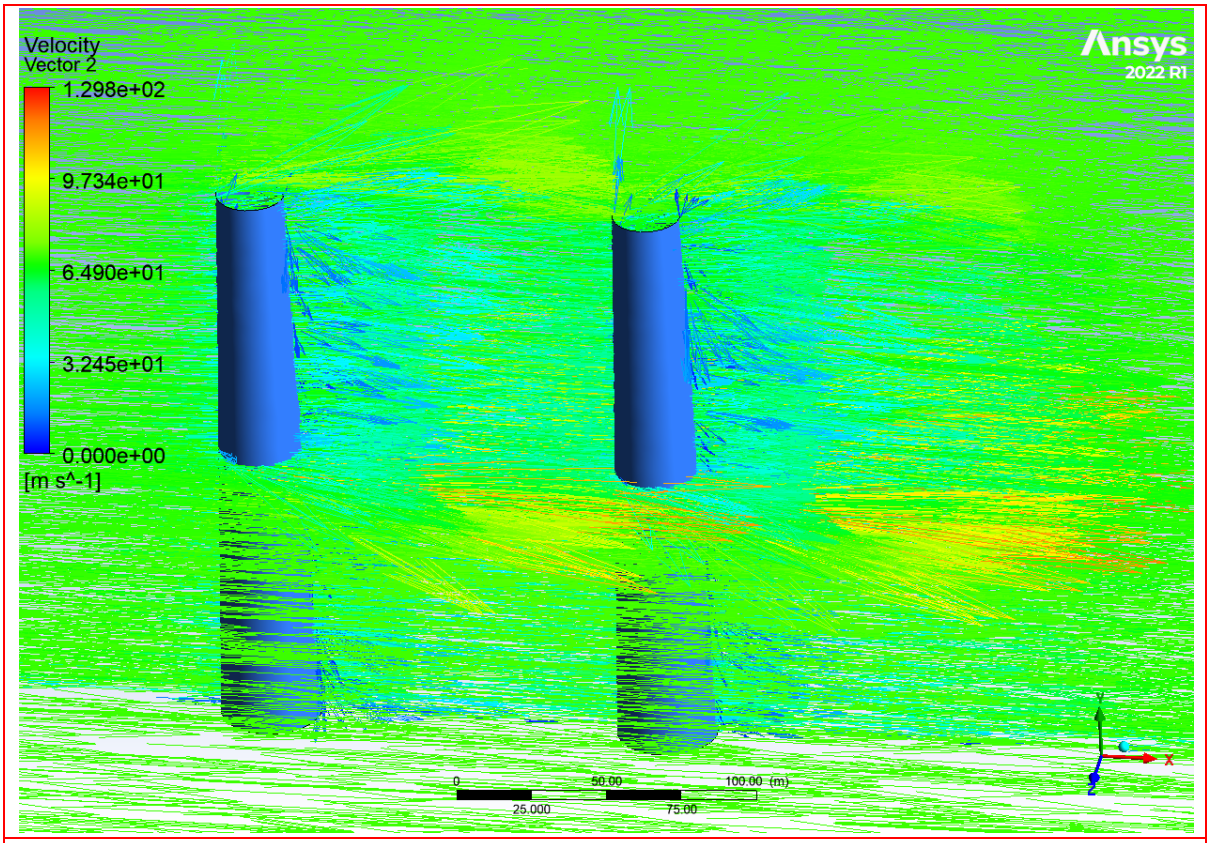

Figure 12. Flow pattern and vortex formation in interference chimney model subjected to wind. (a) front-side, (b) back-side, (c) left-side, and (d) top-side of the interference chimney model

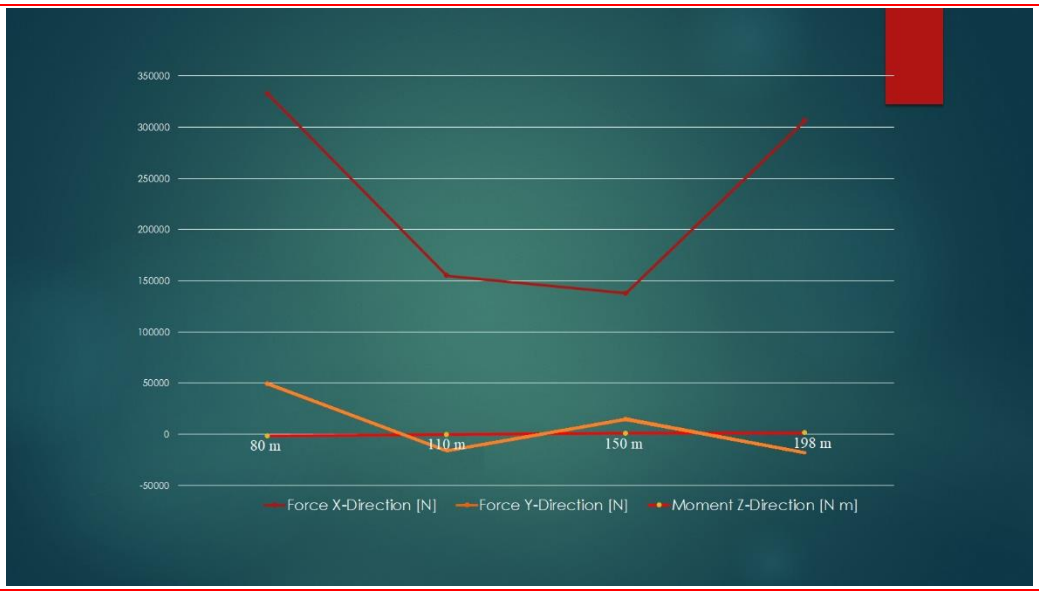

Figure 13. Forces in X and Y direction and Moment in Z direction

5. Conclusion

The correctness of the findings is also dependent on accurately specifying physical characteristic values under actual environment circumstances, modelling in accordance with scale, and properly meshing the model geometry. While the maximum pressure created in the interference chimney model is 2.539*10^3 Pa on the front side and 8.673*10^2 Pa on the leeward side, the maximum pressure developed in the isolated chimney is -9.721*10^2 Pa on the leeward side and 2.534*10^3 Pa on the front side. Whereas the maximum velocity vector in an isolated chimney is 1.101 * 10^2 m/s and the maximum velocity vector in an interference effect chimney is 1.298 * 10^2 m/s.

6. References

1) P. Górski, "Some aspects of the dynamic cross-wind response of tall industrial chimney," *Wind Struct. An Int. J.*, vol. 12, no. 3, pp. 259–279, 2009, doi: 10.12989/was.2009.12.3.259.

2) A. O. Dawood, A. J. Sangoor, and A. H. J. Al-Rkaby, "Behavior of tall masonry chimneys under wind loadings using CFD technique," *Case Stud. Constr. Mater.*, vol. 13, p. e00451, 2020, doi:10.1016/j.cscm.2020.e00451.

3) P. Tranvik and G. Alpsten, "Structural behavior under wind loading of a 90 m steel chimney," *Wind Struct. An Int. J.*, vol. 8, no. 1, pp. 61–78, 2005, doi: 10.12989/was.2005.8.1.061.

4) Khan, M. M., & Roy, A. K. (2017). CFD simulation of wind effects on industrial RCC chimney. *International Journal of Civil Engineering and Technology*, *8*(1), 1008–1020.

5) Khan, M., & Roy, A. K. (2017). Cfd Simulation of Wind Effects on Industrial Rcc Chimney. *International Journal of Civil Engineering and Technology*, *8*(1), 1008–1020. http://www.iaeme.com/IJCIET/index.asp%0Ahttp://www.iaeme.com/IJCIET/issues.asp?JType=IJCIET&VType=8&IType=1

6) Singh, J., & Roy, A. K. (2019a). CFD simulation of the wind field around pyramidal roofed single-story buildings. *SN Applied Sciences*, *1*(11). https://doi.org/10.1007/s42452-019-1476-2

7) Singh, J., & Roy, A. K. (2019b). Effects of roof slope and wind direction on wind pressure distribution on the roof of a square plan pyramidal low-rise building using CFD simulation. *International Journal of Advanced Structural Engineering*, *11*(02), 231–254. https://doi.org/10.1007/s40091-019-0227-3

8) Singh, J., & Roy, A. K. (2019c). Wind Pressure Coefficients on Pyramidal Roof of Square Plan Low Rise Double Storey Building. *Journal of Computational Engineering and Physical Modeling*, *2*(1), 1–15. https://doi.org/10.22115/CEPM.2019.144599.1043

9) Singh, J., & Roy, A. K. (2019d). Wind Pressure Coefficients on Pyramidal Roof of Square Plan Low Rise Double Storey Building. Journal of Computational Engineering and Physical Modeling, 2(1), 1–15. https://doi.org/10.22115/CEPM.2019.144599.1043

10) Roy, A K, Babu, N., & Bhargava, P. K. (2012). Atmospheric Boundary Layer Airflow Through Cfd Simulation on Pyramidal Roof of Square Plan Shape Buildings. *VI National Conference on Wind Engineering*, *February*, 291–299.

11) Roy, A K, Sardalia, A., & Singh, J. (2021). Wind Induced Pressure Variation on High-rise Geometrically Modified Building having Interference through CFD Simulation Wind Induced Pressure Variation on High-rise Geometrically Modified Building having Interference through CFD Simulation. *Computational Engineering and Physical Modeling*, *4*(4), 26–38. https://doi.org/10.22115/cepm.2021.271960.1151

12) Roy, Amrit Kumar. (2010). *Wind Loads on Canopy Roofs* [Ph.D. Thesis, IIT Roorkee, Uttarakhand, India]. http://shodhbhagirathi.iitr.ac.in:8081/xmlui/handle/123456789/1665

13) Chen, B., Cheng, H., Kong, H., Chen, X., & Yang, Q. (2019). Interference effects on wind loads of gable-roof buildings with different roof slopes. *Journal of Wind Engineering and Industrial Aerodynamics*, ***189***(November 2018), 198–217. https://doi.org/10.1016/j.jweia.2019.03.033

14) Chauhan, B. S., Ahuja, A. K., & Rani, N. (2023). *Numerical Response Study of Rectangular Cross-Section Building Under Wind Interference Condition BT - Advances in Structural Mechanics and Applications* (J. A. Fonseca de Oliveira Correia, S. Choudhury, & S. Dutta (eds.); pp. 518–529). Springer International Publishing.

15) Chauhan, B. S., Chakrabarti, A., & Ahuja, A. K. (2022). Study of wind loads on rectangular plan tall building under interference condition. *Structures*, ***43***(January 2020), 105–130. https://doi.org/10.1016/j.istruc.2022.06.041

16) Rukhaiyar, A., Jayant, B., Dahiya, K., Meena, R. K., & Raj, R. (2022). CFD simulations for evaluating the wind effects on high-rise buildings having varying cross-sectional shape. *Journal of Structural Fire Engineering*. https://doi.org/10.1108/JSFE-04-2022-0016